Arabian Journal for Science and Engineering
https://doi.org/10.1007/s13369-024-08747-7

RESEARCH ARTICLE-CHEMISTRY

Biosynthesis of Doped Carbon Dots-Decorated MnO_2 Nanocomposites Using Eucalyptus Extract: Evaluation of Catalytic Activity

Maria Zaib[1] · Kinza Shabir[2] · Tayyaba Shahzadi[2] · Tauheeda Riaz[2] · Indra Neel Pulidindi[3]

Received: 7 July 2023 / Accepted: 11 January 2024

Abstract
In the present work, biosynthesis of two nanocomposites (NC1 and NC2) with different dopants (boron or sulfur) was carried out by utilizing secondary metabolites of *Eucalyptus citriodora* leaf extract for degradation studies of cationic and anionic dyes. Biosynthesized nanocomposites were characterized by UV–Vis spectroscopy, FTIR spectroscopy, SEM imaging, and EDX spectra, which confirmed their functional groups, uniform structure, and the presence of desired dopants. Optimum response for crystal violet dye was observed with 2 mL and 1.5 mL volume, in alkaline medium (pH = 8) at room temperature with dye concentration = 5 mg/L within time interval of 60 and 45 min for NC1 and NC2, while eriochrome black T has shown maximum degradation at 1.5 mL and 1 mL volume in acidic medium at room temperature with 5 mg/L dye concentration in time period of 90 and 60 min for NC1 and NC2. Interference and radical scavenging experiment was performed to elaborate the efficiency and working mechanism of nanocatalysts. The proposed mechanism regarding nanoparticles formation was also discussed.

Keywords Green synthesis · Manganese dioxide nanoparticles · Doped carbon dots · Dye degradation

1 Introduction

In any country, the fundamental industrial units were established to improvise living standards, hence consuming enormous supplies of water resources in their operational procedures [1]. As per reported studies of United Nation World Water Development (UNWWD), drinking water shortage is already established. About 748 million people is unaware of this fact, and continued increasing demands by world manufacturing industries up to 400% seriously threatened the situation. Another 400% increase is to be expected by year 2050 [2].

Hygienic and healthy lifestyle of human beings depends on water resources. All kind of activities performed at any level ultimately consumed water in one form or another [3, 4]. Anthropogenic activities and enormous population growth caused contamination of water resources. This global issue will have stronger impact in future leading to water scarcity challenges [2, 3]. Various industries such as food, pharmaceutical, leather, cosmetics, etc., has been releasing untreated wastewater containing dyes into the surrounding environment. Further, about 15% of dye consumed is also lost during the industrial processes and contributes as a water pollution source [2].

Dyes are chemical compounds capable of imparting color to a variety of substrates. Light absorption in visible range (400–800 nm) produced color due to interaction of electromagnetic radiations with electronic system of dyes. Dyes are complex molecules mostly show distinctive nature along with resistive response toward heat and detergents. Their detection is challenging even at low concentration. Sunlight penetration is restricted due to the undesirable colorful discharges in hydrospheric surfaces. Hence, biological and photochemical lives have been compromised. Dyes can act as potent source of water contamination due to its toxic, teratogenic, mutagenic and carcinogenic nature. Ultimately, they can be health hazards to various human organs such as central nervous system, liver, brain and kidney [4, 5].

One of the prime challenges is remediation of toxic dyes containing wastewater. As per major concern, researchers

✉ Maria Zaib
mariaa.zaib@gmail.com

1 Department of Chemistry, University of Jhang, Jhang 35200, Pakistan

2 Department of Chemistry, Government College Women University Sialkot, Sialkot 51310, Pakistan

3 School of Science, GSFC University, Vadodara, India

Published online: 16 February 2024

have made many efforts for the treatment of dye containing industrial effluents [6]. Traditional techniques including electrochemical reduction, membrane filtration, chemical sedimentation, ion exchange and adsorption have demonstrated potential for the treatment of dye containing effluents. Nonetheless, there is no technique available for universal treatment and application. Every process has its own pros and cons [7]. In order to cater intensive demand for converting contaminants into environmental benign candidates, highly effective and progressive modern technology is required by adopting optimum requirements and approaches. Biocompatible nanocomposites have illustrated capacity to degrade dye into simpler forms that could be a useful nutrient supplier for various microorganisms present in the ecosystem [8].

In this perspective, carbon dots have earned a renowned position than metal quantum dots. They could be easily prepared in one step, with minimum cost impact. Further, carbon dot exhibited adequate aqueous solubility, improved functionalization, chemical inertness, biocompatibility, and fluorescent phenomenon. Despite the fact that quantum dots have many biomedical applications, these are expensive nanostructures and impart toxic side effects [9].

Carbon-based catalysts have two categories as bare carbon dots and composite carbon dots. Bare carbon dots catalyst is only single catalyst without any incorporated material. Bare carbon dots have been reported as metal free catalyst and employed for degrading bromothymol blue and thymol blue in the presence of hydrogen peroxide. Composite carbon dots are doped with several types of material (non-metal or transition metal). Carbon dot/titania nanocomposite was reported to be the promising candidate for photocatalytic degradation of methylene blue dye [10].

Heteroatom introduced into carbon dots framework can easily improve the chemical features associated with internal and external carbon dot framework. Generally, heteroatom doping is an effective approach for altering electronic features and giving new active sites to carbon dots [11]. Band gap could also be tuned on the basis of energy difference in surface states and valence band [12]. According to reported literature studies, heteroatomic doping in carbon dots has extended their applications to fluorescence sensing, anti-counterfeiting encryption and light emitting diodes [13, 14].

In this study, novel nanocomposites of metal oxide nanoparticles and doped carbon dots were prepared through a green process by using *Eucalyptus citriodora* aqueous leaves extract. Influence of different dopants (boron or sulfur) on the preparation of doped carbon dots and their comparative effect on the activity of nanocomposite for crystal violet and eriochrome black t dye degradation was analyzed.

More than five hundred species of this plant are available from shrubs to trees. This plant popularly, known as gum tree [15], is abundantly available in all regions of Pakistan [16]. *Eucalyptus* genus belonged to Myrtaceae family. These plants are evergreen and perennial. *E. citriodora* comprises phenolic compounds such as catechin, chlorogenic acid, gallic acid and protocatechuic acid [17, 18]. This plant is known to contain reductant molecules, and their volatile oils are considered to be rich source of 1,8-cineole also known as α-monoterpene or eucalyptol [16].

2 Experimental Section

2.1 Chemicals

Potassium permanganate ($KMnO_4$), boric acid (H_3BO_3), sodium thiosulfate ($Na_2S_2O_3$), acetic acid (CH_3COOH), sodium hydroxide (NaOH), sodium nitrate ($NaNO_3$), phosphoric acid (H_3PO_4), nitric acid (HNO_3), crystal violet (CV), eriochrome black T (EBT), hydrochloric acid (HCl), methanol (CH_3OH) and ethanol (C_2H_5OH) were purchased from Merck with $\geq$ 99.9% purity. All chemicals and reagents used in this study were of analytical grade and utilized as received.

2.2 Collection and Preparation of Plant Extract

Fallen leaves of *E. citriodora* plant were collected as green precursor from Government College Women University, Sialkot (32.50°N, 74.53°E). Collected leaves were washed properly by distilled water for removing their surface dirt particles and impurities. Leaves were then shade dried. After obtaining well-dried leaves, these were grinded into fine powder and stored for further utilization. About 4 g prepared powder of leaves was added into 100 mL distilled water in a 200 mL beaker. This beaker was then placed on magnetic hotplate for proper heating at 70 °C for half an hour with continuous stirring. After filtering this mixture, plant extract was stored and kept at 4 °C [16].

2.3 Biosynthesis of Manganese Dioxide Nanoparticles

Green synthesis of metal dioxide nanoparticles was carried out by the reported method with some modifications [19]. In a 250-mL beaker, 10 mL liquid plant extract was mixed with 100 mL of 0.1 M $KMnO_4$ solution under constant stirring conditions for three hours at room temperature. After stirring, the dark brown solution was sonicated for 30 min in order to ensure homogeneity. At the bottom of beaker, solid dark brown manganese dioxide nanoparticles were settled down. Centrifugation was carried out for proper washing and separating nanoparticles. After washing, solid nanoparticles were dried below 100 °C for approximately two hours in hot air oven.

2.4 Green Synthesis of Sulfur-Doped Carbon Dots

Sulfur-doped carbon dots (SCDs) were prepared by dissolving the measured amount of dopant and plant extract according to already reported green method with few modifications [20]. Briefly, about 0.35 g of sodium thiosulfate (as sulfur source) was dissolved in 5 mL plant extract. The mixture solution was microwave-irradiated (Dawlance DW-210, 750W) at 750W for 4 min. After irradiation, solution was prepared by dissolving resultant solid particles into 15 mL distilled water. The solution was stirred for 10 min and centrifuged for 30 min. Finally, SCDs were collected as light brown colored supernatant.

2.5 Green Synthesis of Boron-Doped Carbon Dots

Typically, 1 g boric acid was dissolved into 10 mL plant extract. The reaction mixture was subjected to ultrasonication for 10 min. After that, reaction mixture was microwave-irradiated at 750W for 5 min. Final solid product was dissolved in 20 mL distilled water, stirred for 10 min and centrifuged for 30 min. Finally, biosynthesized yellowish color supernatant was collected as BCDs [21].

2.6 Preparation of Nanocomposites

Initially, Britton-Robinson Buffer (BR Buffer) was prepared by mixing equal volumes (10 mL each) of acetic acid, boric acid, phosphoric acid and 0.01 M NaOH solution to adjust the pH of the mixture [22]. 200 mg/L of solid manganese dioxide nanoparticles was redispersed in distilled water. To prepare the nanocomposite, equal volume of doped CDs, manganese dioxide nanoparticles (200 mg/L) and 18 mL of BR Buffer was taken in a glass beaker. Then, reaction mixture was sonicated for 5 min. Finally, green-synthesized doped carbon dots/manganese dioxide nanocomposite was stored at 4 °C [23].

2.7 Characterization of Doped Carbon Dots/Manganese Dioxide Nanocomposites

Optical characteristics of prepared materials were analyzed via UV–Vis spectrometer (Specord Plus 200, Analytica Jena, Germany) within the range of 200 nm to 500 nm. FTIR spectra were recorded in the range of 4000 cm^{-1} to 500 cm^{-1} by using Nicolet 6700 FTIR spectrophotometer (Thermo Fischer Scientific, US). SEM with EDX analysis (Tescan Vega3, Czechia) was performed with magnification of 50 kX, 25 kX, 10 kX and 5 kX at scale level 500 nm, 1 μm, 2 μm and 5 μm.

2.8 Point Zero Charge (PZC) Measurement

In order to determine the point zero charge of nanocomposite, 0.1 M solution of $NaNO_3$ was prepared and 40 mL of this was taken in different test tubes. Then, 1 mg of nanocomposite was added to each test tube after adjusting pH of each solution within 3–13 by using solutions of 0.1 M NaOH or 0.1 M HNO_3. pH of respective solutions was noted before and after the 24-h contact time and labeled as pHi and pHf, respectively. The difference between initial and final pH was taken as ΔpH. Then, graphical plot was drawn between pHi and ΔpH in order to find the PZC value, respectively [24].

2.9 Dye Degradation Studies

Nanocomposites were employed for evaluating catalytic degradation study of cationic and anionic dyes separately. Different parameters such as volume of nanocomposite, pH of dye solution, temperature, contact time and concentration were studied and optimized. In all these experiments, degradation percentage was calculated by the following formula:

$$\text{Degradation } \% = \frac{\text{Initial Absorbance} - \text{Final Absorbance}}{\text{Initial Absorbance}} \times 100 \quad (1)$$

3 Results and Discussion

3.1 Characterization

3.1.1 UV–Visible Spectroscopic Analysis

Two unique and strong absorption peaks of biosynthesized nanoparticles were observed in spectral region of 200–800 nm. These bands with maximum absorbance values were the clear indicator for fabricated nanoparticles. In Fig. 1a, the first peak can be seen at λ_{max} value of 210 nm and the second broad peak at 292 nm, respectively. As per reported literature, MnO_2 exhibits broad UV–Vis peak between 250 to 700 nm and a subsidiary peak at 210 nm [25]. Symmetrical spectrum indicated the monodispersed nature of manganese dioxide nanoparticles [26, 27].

The optical absorption peaks of doped carbon dots were observed in mostly UV region (200 nm–400 nm), but its tail can be extended to visible region of spectrum within the range of 400–800 nm. It is the characteristic of doped carbon dots to give distinctive absorption peaks in 200–400 nm range [28].

Boron carbon dots were prepared by green precursor plant extract as carbon source and boric acid as a boron dopant. Boron influenced the carbon electronic configuration in a

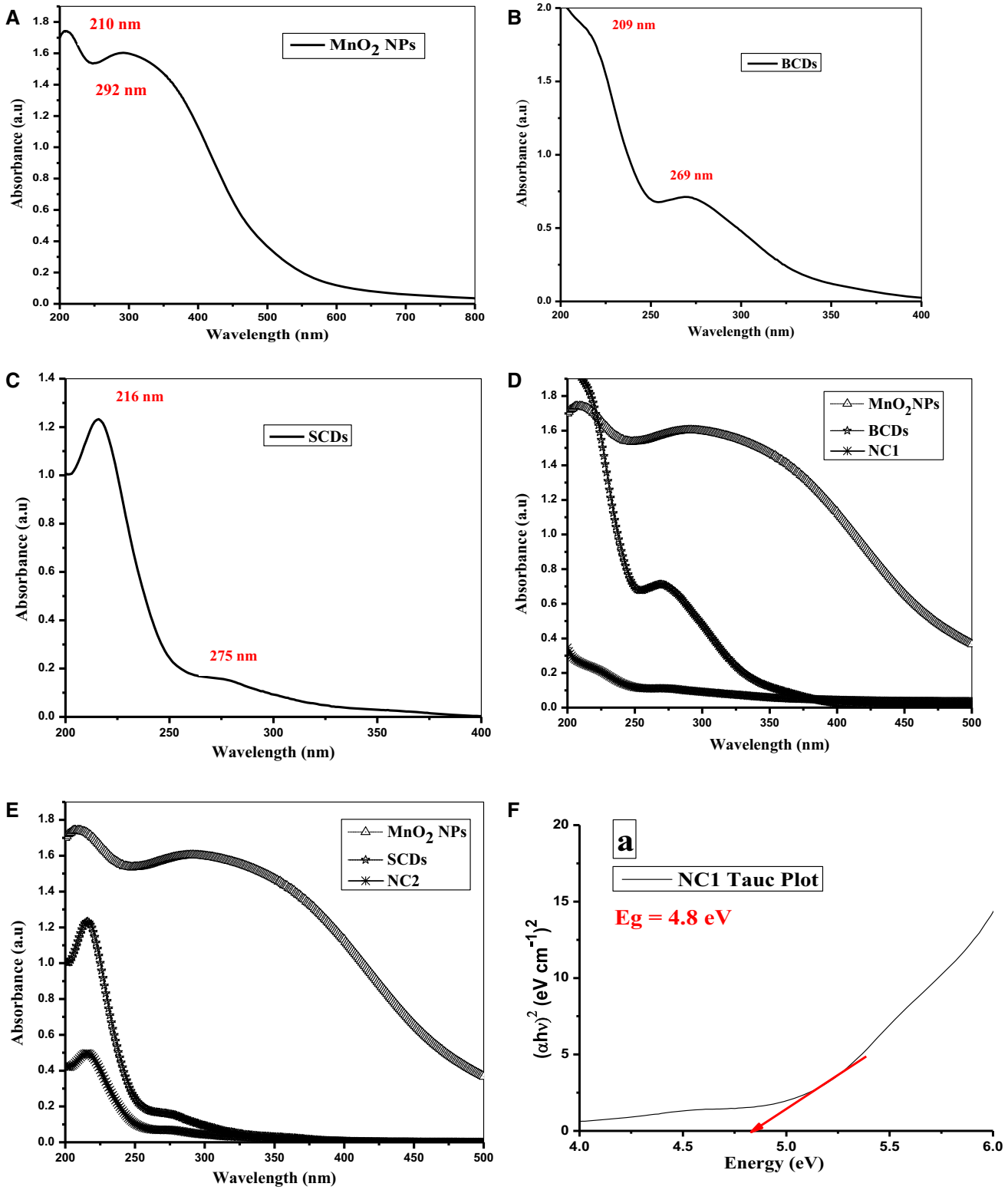

Fig. 1 UV–Vis spectra of MnO_2 nanoparticles (**a**), boron-doped carbon dots, (**b**) sulfur-doped carbon dots (**c**), spectra overlay of MnO_2, BCDs and NC1 (**d**) spectra overlay of MnO_2, SCDs and NC2 (**e**), band gap energy graph of NC1 (**f**) and NC2 (**g**)

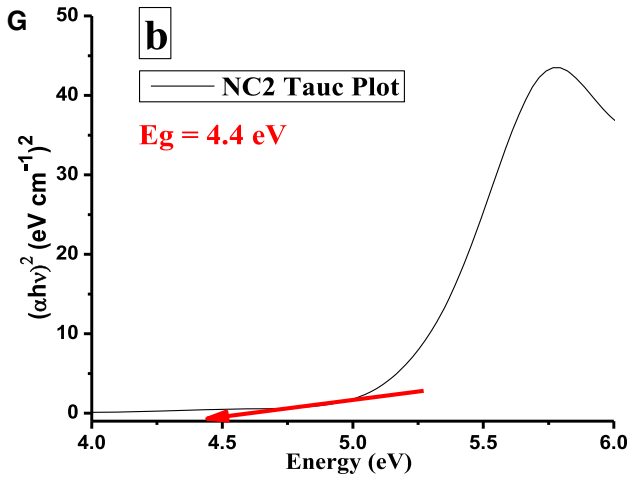

Fig. 1 continued

preferable catalytic way. It is p-type dopant for carbon core and creates vacant positions like electron-deficient situation in doped carbon dots that created surface defects, hence improving catalytic activity [29]. Boron-doped carbon dots show two unique and distinctive peaks in Fig. 1b within 200–400 nm range.

First weak shoulder absorption peak at 209 nm corresponds to $\pi \rightarrow \pi^*$ transition where π electron shifting occurs and indicates C=O presence in carbon skeleton of sp^2 aromatic carbon domain. Second typical peak at 269 nm is correlated with transitions of $n \rightarrow \pi^*$ in surface groups like C=O bond containing oxygen groups along with conjugated diene (=C–C=) structure of doped carbon dots [12].

Sulfur-doped carbon dots were prepared by using plant extract (carbon sources) and sodium thiosulfate as sulfur dopant. It would be catalytically more efficient and favorable dopant in enhancing optical properties of doped carbon dots. It is n-type dopant and provides extra electrons to the carbon framework [30]. Sulfur-doped carbon dots show two absorption peaks. Figure 1c shows the first sharp peak at 216 nm.

This represents $\pi \rightarrow \pi^*$ electronic transition of aromatic (C=C) group with carbon skeleton exhibiting sp^2 domain, while the second one is weak peak around about 275 nm. This can be correlated to $n \rightarrow \pi^*$ transitions of carbonyl group (C=O) and C–S bond in conjugated system of sulfur-doped carbon dots. Hence, this depicts the presence of heteroatomic surface sites [20].

Nanocomposite (NC1) shown in Fig. 1d was biosynthesized by using boron-doped carbon dots and metal dioxide nanoparticles. Nanocomposite (NC2) depicted in Fig. 1e was green-synthesized by using sulfur-doped carbon dots and manganese dioxide nanoparticles.

NC1 or NC2 exhibited the optical properties in UV–Vis region between 200 and 500 nm. Both composite displayed the hypochromic effect or blue shift in wavelength due to electrostatic interaction between doped carbon dots and MnO_2 NPs, hence confirming the formation of blended and newly prepared nanocomposite. NC1 showed blue shift absorption peak at λ_{max} of 260 nm compared to absorption peaks of manganese dioxide nanoparticles (292 nm) and boron-doped carbon dots (269 nm). NC2 depicted λ_{max} value of 268 nm as compared to absorption peaks of manganese dioxide nanoparticles (292 nm) and sulfur-doped carbon dots (275 nm). NC1 or NC2 spectral analysis also confirmed that dopant embedded successfully with nanoparticles. Electrostatic interaction within doped carbon dots and MnO_2 NPs also helps in improving their role for catalytic activity [31].

Band gap energy values were evaluated by using Eq. (2):

$$(\alpha hv)^n = K(hv - Eg) \tag{2}$$

where α is absorption coefficient, n is index or optical transition of semiconductors so $n = ½$ for direct band gap semiconductor, K is proportionality constant depends on material, hY is photon energy in eV and Eg is band gap. Tauc plot was drawn between $(\alpha hv)^2$ versus energy (eV). Band gap values of both NC1 and NC2 (Fig. 1f and g) were calculated by extrapolating linear portion of Tauc plot which cuts energy axis at $\alpha = 0$. Estimated optical band gap energy value for NC1 and NC2 was 4.8 eV and 4.4 eV, respectively. In comparison to NC1, NC2 depicted a higher red shift value. This reduction can be attributed to the more induced energy band edge bending caused by sulfur doping. Further, sulfur doping facilitated the creation of new energy bands near the conduction band to a greater extent [32].

3.1.2 Fourier Transform Infrared (FTIR) Analysis

FTIR analysis has been carried out to study the surface data profile of specific functional groups pertaining to biomolecules that have been involved in preparation of nanocomposites.

FTIR spectroscopic characterization was performed within 4000–650 cm^{-1} range. In spectrum of NC1 (Fig. 2a), various functional groups are confirmed such as strong absorption band by stretching vibration of –OH (3338 cm^{-1}), stretching absorption peak of Ar–H or = C–H (2970 cm^{-1}) and –CH (2912 cm^{-1}) which can also be observed. Two absorption peaks are also observed that confirmed the presence of embedded BCDs which appeared as B–O–C (2133 cm^{-1}) and B–O stretching vibration (2101 cm^{-1}). Sharp absorption of carbonyl was also observed at 1653 cm^{-1} which improved the hydrophilic nature of nanocomposite. Aromatic carbon core was observed by C=C stretching vibration at 1636 cm^{-1}. Carboxyl functionality gave peak at 1340 cm^{-1}. C–B stretching vibration appeared at 1134 cm^{-1}. Carbon dots core also showed asymmetric stretching of

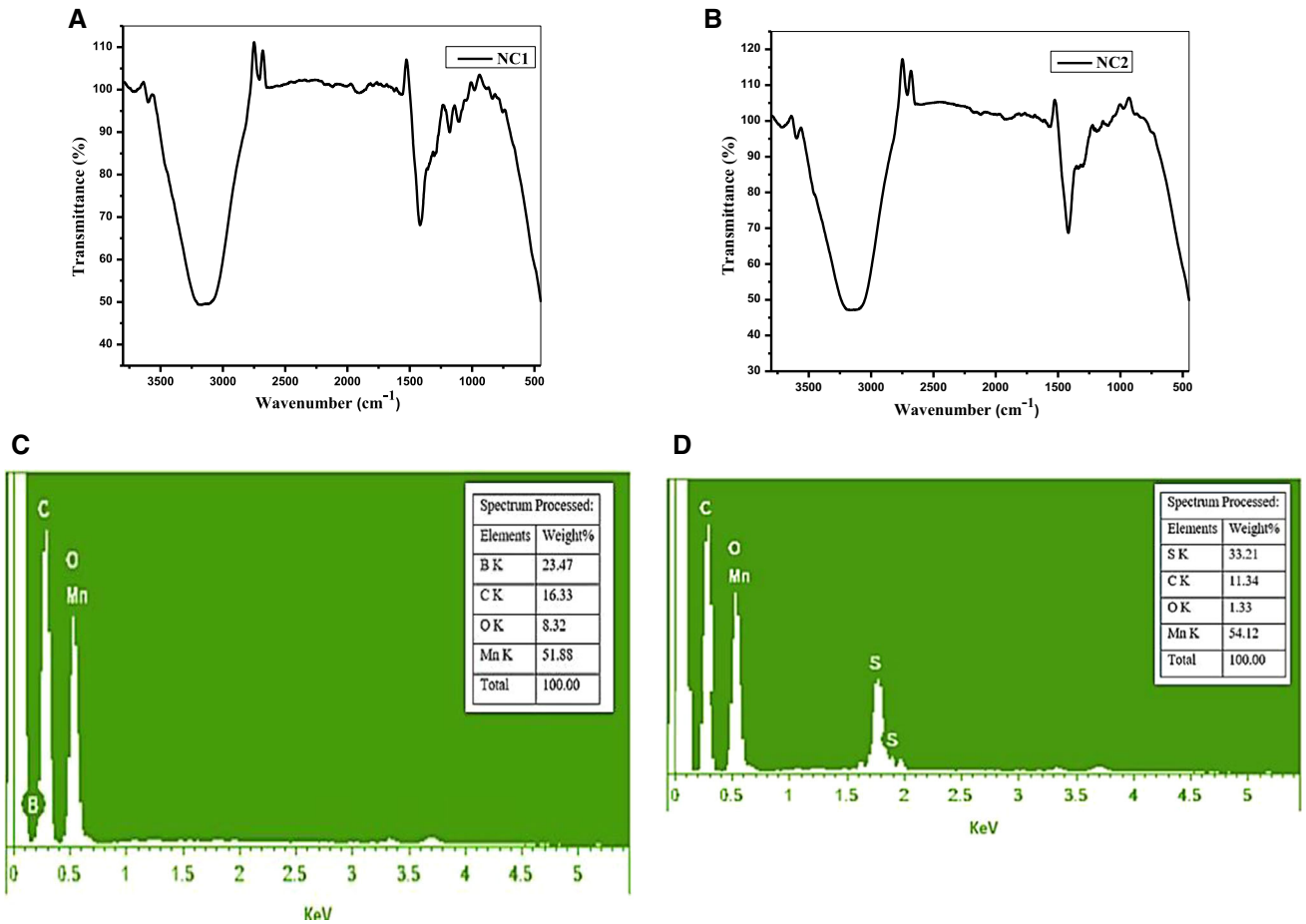

Fig. 2 FTIR spectra of NC1 (**a**) and NC2 (**b**) EDX spectrum of NC1 (**c**) and NC2 (**d**)

C–OH or C–O, and this connotes the deformation in aliphatic ether or of primary and secondary alcoholic groups at 1080 cm^{-1}. O–H out-of-plane vibration was also observed at 822 cm^{-1}. Peaks representing B–O–H/Mn–OH bond appeared at 780 cm^{-1}. Spectrum also showed new peak of B–Mn bonding at 766 cm^{-1}. Strong stretching collision of O–Mn–O is observed at 719 cm^{-1}. Distinctive and confirmatory stretching vibration of Mn–O bond (677 cm^{-1}) is also observed [26, 27, 29].

Nanocomposite (NC2) was being prepared by decorating manganese dioxide nanoparticles with sulfur-doped carbon dots. FTIR sample was run within range of about 4000–650 cm^{-1} and resulting spectrum of NC2 shown in Fig. 2b. Stretching vibration of hydrogen-bonded hydroxyl is shown by absorption band at 3339 cm^{-1}. Prominent vibrational peaks were observed such as S–H bond in carboxyl group at 2149 cm^{-1}. Stretching vibration ascribed to peak of C=S appeared around 2133 cm^{-1}. Asymmetric stretching vibration mode of C–S at 2116 cm^{-1} and symmetric vibration peak of C–S–C are observed at 1993 cm^{-1}. C=O illustrated peak at 1792 cm^{-1}. Aromatic or unsaturated system exhibits pronounced symmetric stretching vibrations of C=C around 1653 cm^{-1}. Hydrocarbon core content of carbon dots appeared by C–H stretching vibration at 1636 cm^{-1}. Carboxyl moiety is shown at 1340 cm^{-1}. Mn–OH vibration appeared at 1121 cm^{-1}. MnO_2 nanoparticles are confirmed by bending vibration mode and stretching collision peak of O–Mn–O which appeared at 670 cm^{-1} [20, 26, 33].

Common peaks of carboxyl, carbonyl and hydroxyl functionalities over the both composite surface depicted that biomolecule of plant extract successfully enriched, stabilized and capped the composite, hence enhancing the nanocomposite catalytic efficiency. Resulting significant spectrum of NC1 or NC2 nanocomposite shows that characteristic features of BCDs or SCDs have successfully decorated the manganese dioxide nanoparticles and verified formation of the nanocomposite.

3.1.3 Energy Dispersive X-ray (EDX) Analysis

EDX analysis is conducted for examining elemental composition of NC1 and NC2 (Fig. 2c and d).

Each peak of graph signifies the specific quantified number of elements present within composite. In Fig. 2c, all peaks

coordinated to boron-doped carbon dots-decorated manganese dioxide nanocomposite, hence indicating the absence of impurity in it. EDX spectrum depicted the main strong peaks of boron (B), carbon (C), oxygen (O) and manganese (Mn) with 23.48%, 16.33%, 8.32% and 51.88% percent content, respectively. EDX spectrum of NC2 depicted in Fig. 2d shows signals of sulfur (S), carbon (C), oxygen (O) and manganese (Mn) with 33.21%, 11.34%, 1.33% and 54.12% percent content, respectively. Line type of K series has been shown by EDX spectra in both the cases. This shows that electrons resided within K shell series and nearer to the nucleus. K line emission shown by NC1 or NC2 has been associated with Kα. EDX spectra have shown the uniform distribution of elemental composition within NC1 or NC2 sample [2, 34, 35].

3.1.4 Scanning Electron Microscopy (SEM) Analysis

Scanning electron microscopic analysis is employed to evaluate the surface morphology and composition of prepared materials [36, 37]. SEM photographs of NC1 in Fig. 3a–d revealed even distribution of amorphous spherical MnO_2 nanoparticles throughout nanosheet matrix. SEM images of NC2 in Fig. 3e–h illustrated crystalline nanospheres of MnO_2 nanoparticles uniformly embedded within homogenous matrix of sulfur-doped carbon dots in the newly prepared composite. In both cases, at lower-magnification power, irregular and heterogeneous dispersion was observed. This might be due to biomolecules of leave extract, while at higher magnification power, images depicted slight regular, equal and homogenous distribution. Both NC1 and NC2 depicted well-embedded doped carbon dots and MnO_2 nanoparticles-based composite [26, 37, 38].

3.2 Comparative Catalytic Degradation Studies of Dyes

Comparative catalytic degradation studies of both cationic and anionic dyes were studied by utilizing boron-doped carbon dots-decorated manganese dioxide nanoparticles (NC1) and sulfur-doped carbon dots-decorated manganese dioxide nanoparticles (NC2). Crystal violet (CV) as a cationic dye and eriochrome black T (EBT) as anionic dye have been selected as model, and their degradation efficiency was observed in detail. Different optimizing parameters like volume of nanocomposite, pH of dye solution, temperature of dye solution, dye concentration in solution and contact time have been analyzed and delineated.

In order to assess optimum reaction parameters for dyes degradation studies, UV–Vis spectrophotometer (Specord 21s0 plus, Analytic Jena AG, Germany) has been utilized. Absorbance values were recorded for both cationic and anionic dyes at $\lambda_{max} = 590$ nm for CV and $\lambda_{max} = 554$ nm for EBT, respectively.

3.2.1 Effect of Nanocomposite Volume

In order to study the effect of nanocomposite volume in catalytic degradation of dyes, different volumes (0.25 mL, 0.5 mL, 1 mL, 1.5 mL and 2 mL) of both NC1 and NC2 were tested with 25 mL of cationic or anionic dye solution having concentration 5 mg/L at room temperature for maximum contact time of about 24 h. By using spectrophotometer, initial absorbance (Ai) was noted for all the dye solutions before adding nanocomposite. After 24 h, final absorbance (A_f) was noted and % degradation was calculated and shown in Fig. 4.1a, b.

In case of crystal violet-cationic dye (Fig. 4.1a), maximum percentage degradation of 70% and 92% was observed at 2 mL and 1.5 mL for NC1 and NC2, respectively. In case of EBT (Fig. 4.1b), maximum percentage degradation of 35% and 39% was observed at 1.5 mL and 1 mL for NC1 and NC2, respectively.

In the beginning, lower degradation percentage was observed that gradually increases till the attainment of an optimized value. Afterwards, degradation efficiency was found to be decreased with increasing volume of respective nanocomposite. Decreased dye degradation in the initial phase was due to lesser reactive species generated by fewer electron–hole entities in the aqueous reaction mixture. Increased degradation trend was observed owing to increased generation of more reactive species facilitated by higher concentration of NC1 or NC2 in the reaction mixture. Hence, higher volume values of the nanocatalysts favor the degradation of both dyes. After the optimum response, further increase in volume of nanocomposite decreased the degradation efficiency. This is due to the agglomeration phenomena that increased the particle size leading to reduced surface area and surface active sites.

NC2 showed better degradation percentage and catalytic activity with both types of dyes as compared to NC1. This is because NC2 was more active catalyst on the basis of optical band gap energy value. Reducing band gap value can extend the energy range of photoexcitation and thus leads to enhanced photodegradation process [1].

3.2.2 Effect of Dye Solution pH

Catalytic activity of NC1 and NC was also investigated under various pH conditions within range of 2–10. In order to calculate optimized pH value, both cationic and anionic dye in all types of pH environment was studied with constant remaining experimental parameters. Graph between % degradation and dye solution pH is plotted and shown in Fig. 4.2a, b.

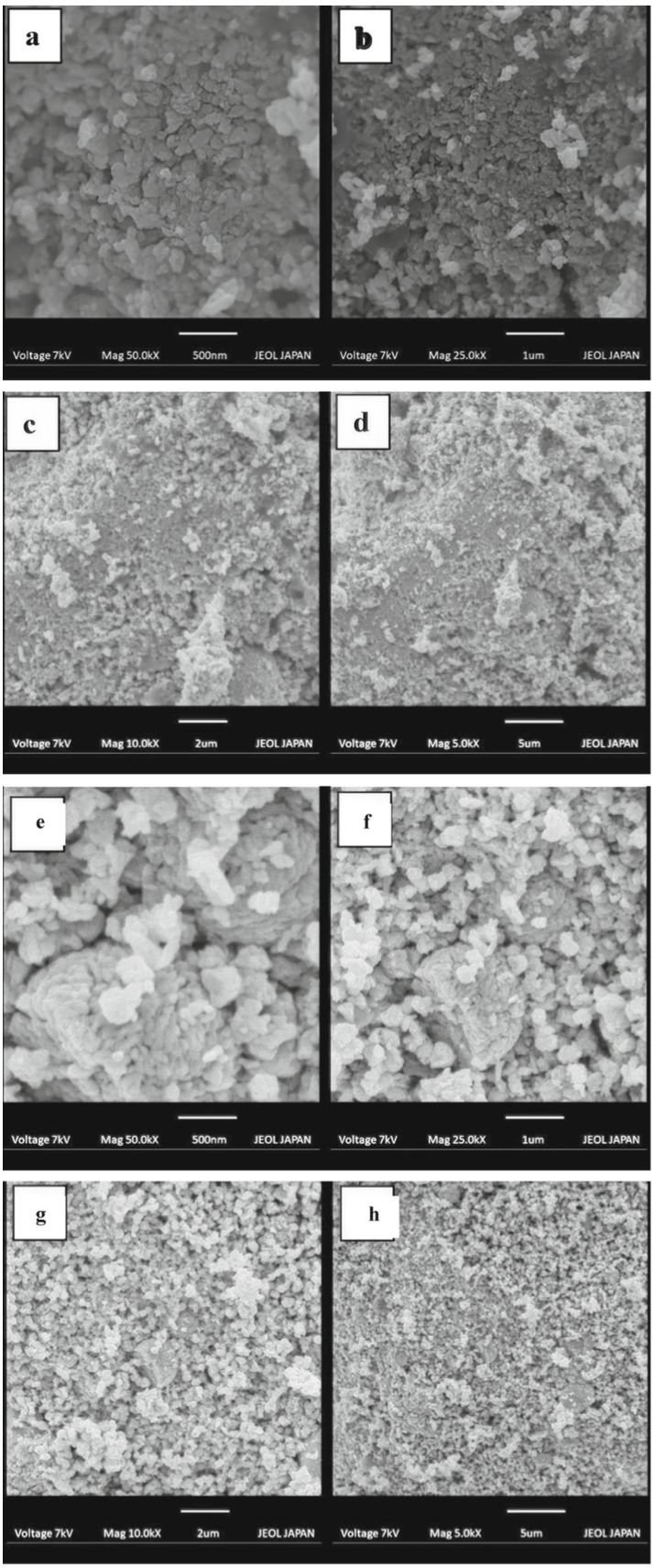

Fig. 3 SEM images of NC1 and NC2 at scale of (**a**, **e**) 500 nm (**b**, **f**) 1 μm (**c**, **g**) 2 μm and (**d**, **h**) 5 μm

Fig. 4.1 a, b

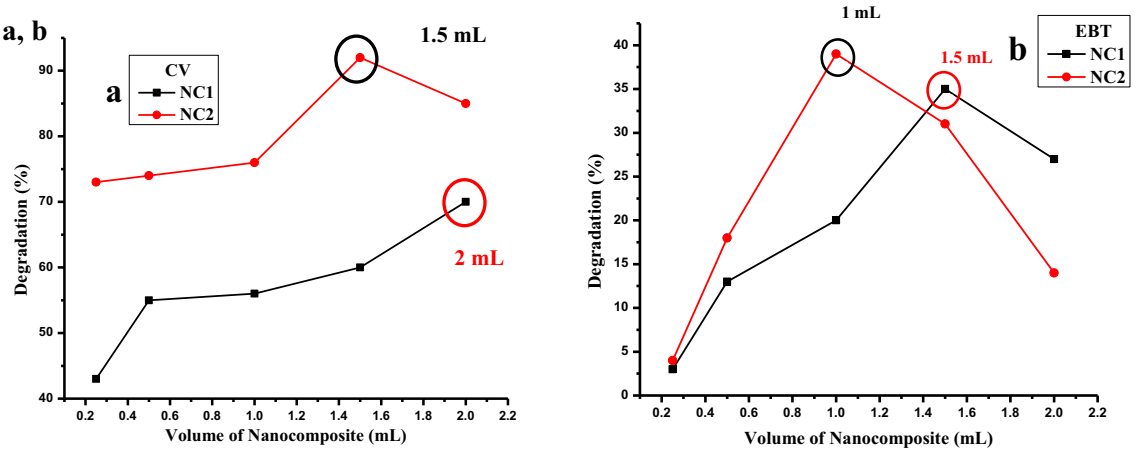

Fig. 4.2 a,b

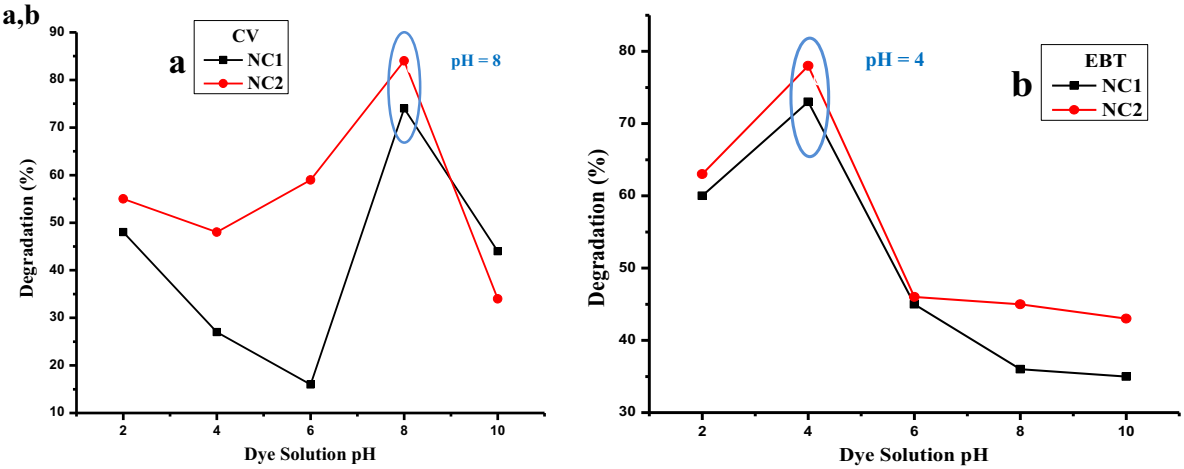

Fig. 4.3 a,b

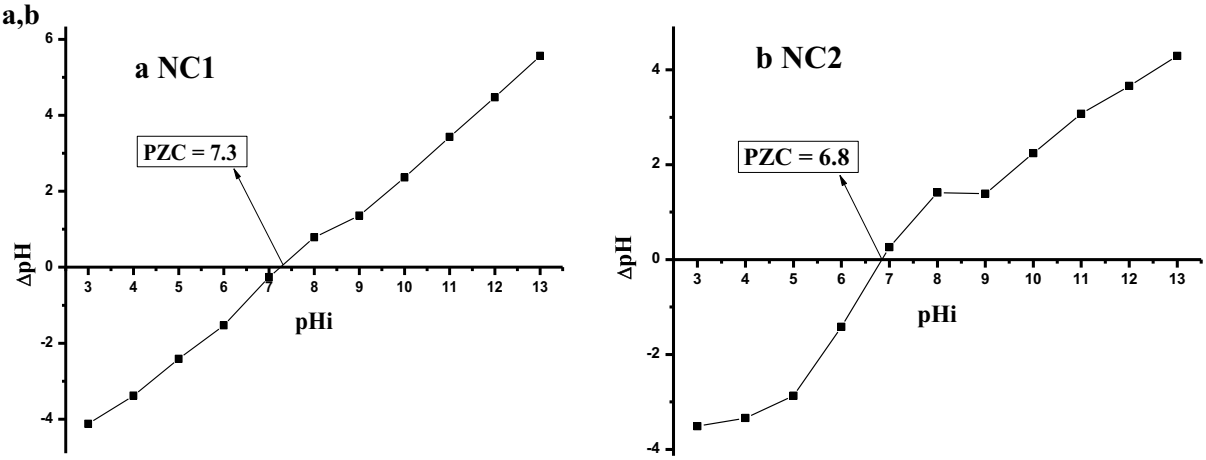

Fig. 4 1: Effect of nanocomposite volume on degradation studies of CV (**a**) and EBT (**b**), 2: Effect of dye solution pH on degradation studies of CV (**a**) and EBT (**b**), 3: Point zero charge calculations for NC1 (**a**) and NC2 (**b**), 4: Effect of dye concentration and time on degradation studies of CV (**a**, **b**) and EBT(**c**, **d**), 5: Effect of temperature on degradation studies of CV (**a**) and EBT (b), 6: Interference studies for CV (**a**) and EBT (**b**), 7: Scavenging radical study for CV (**a**) and EBT (**b**)

Fig. 4.4 a,b

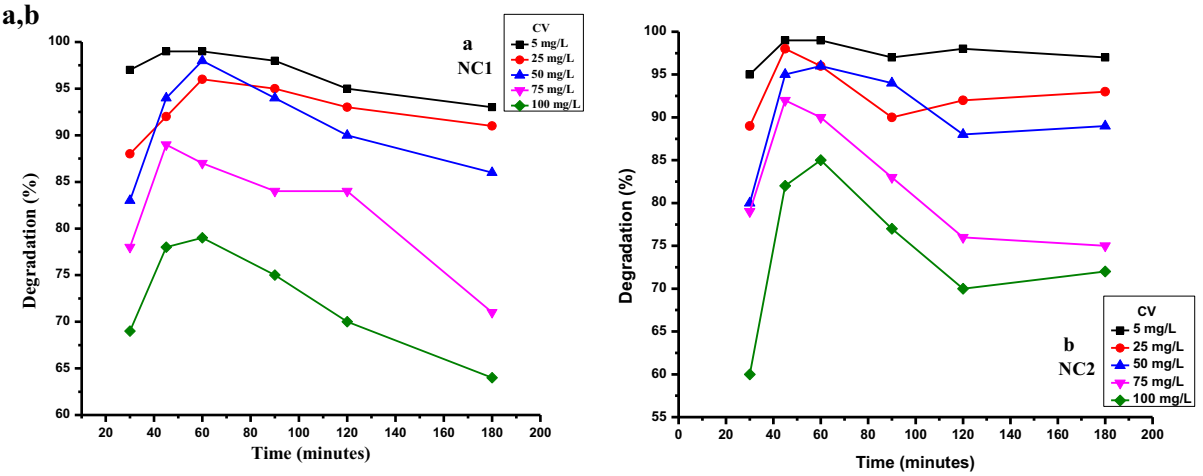

Fig. 4.4 c,d

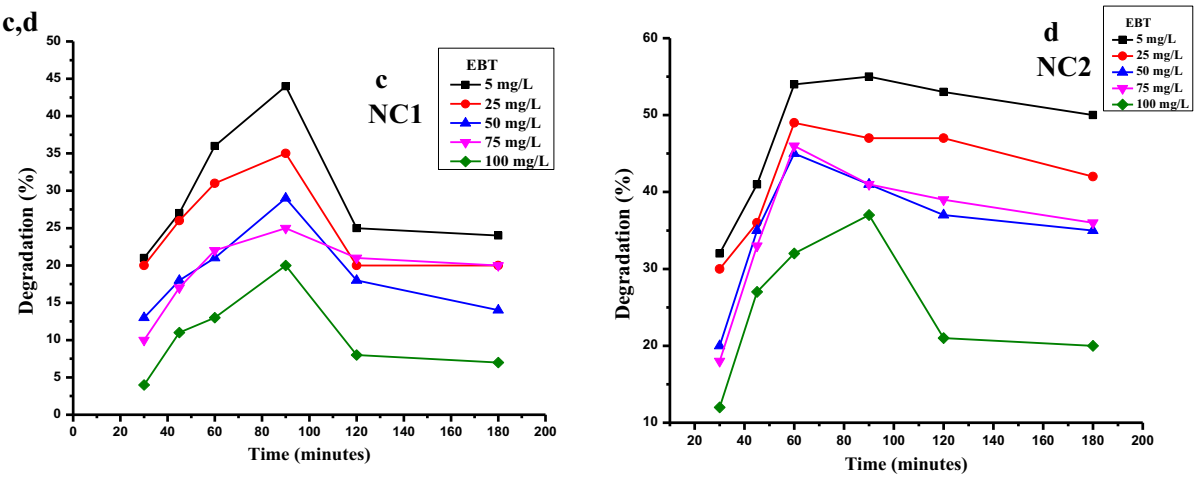

Fig. 4.5 a,b

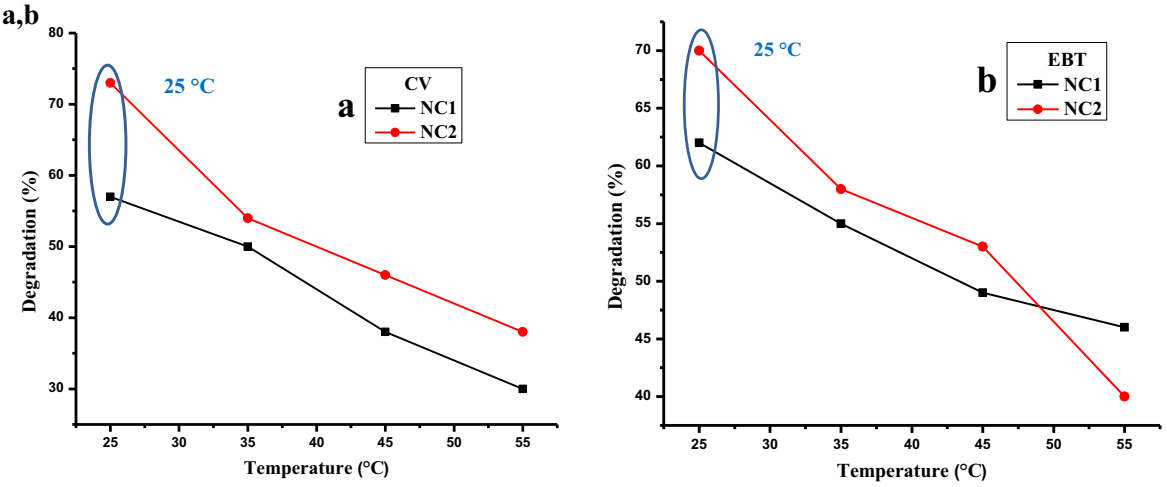

Fig. 4 continued

Fig. 4.6 a,b

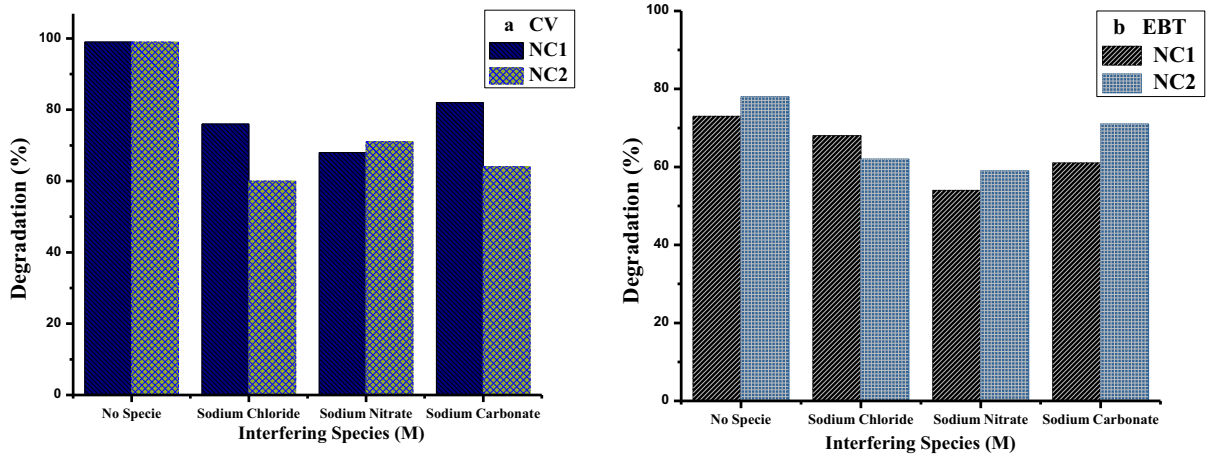

Fig. 4.7 a, b

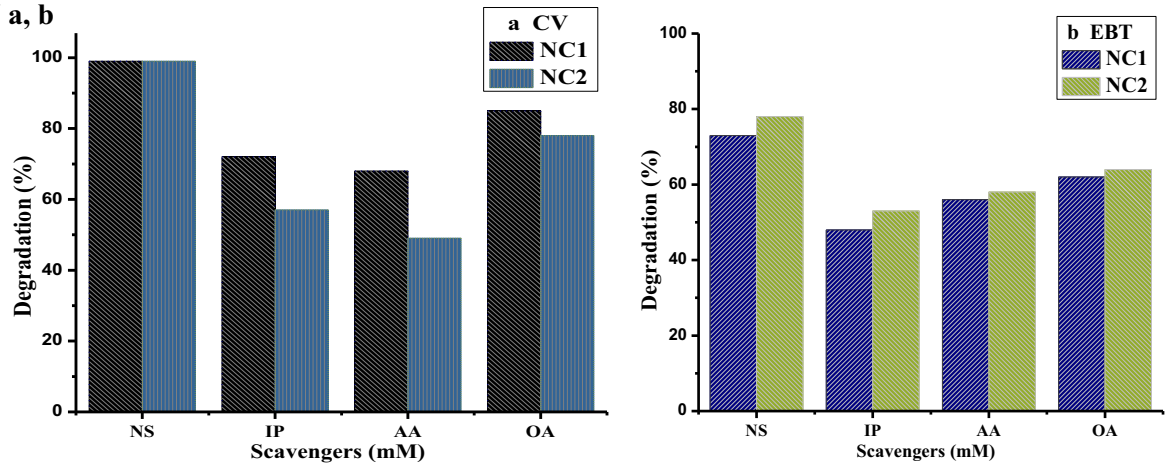

Fig. 4 continued

NC2 illustrates better degradation percentage and catalytic activity with both types of dyes as compared to NC1. Maximum degradation of about 85% and 74% at pH 8 (in alkaline media) was observed for cationic dye by NC2 and NC1, respectively, while in case of anionic dye, degradation percentage of about 78% and 73% at pH 4 (in acidic media) was examined for NC2 and NC1, respectively.

In case of CV dye, hydroxyl radicals (OH·) are predominantly involved in degradation procedure (discussed further in radical scavenging experiment) and these are formed by the reaction of holes (h^+) with hydroxyl ions (OH^-) (Scheme 1).

Under acidic medium, primarily present photogenerated holes (h^+) and minor quantity of hydroxyl ions (OH^-) attributed to lower number of hydroxyl radicals (OH·). Hence, under low pH conditions, minimum dye degradation percentage is attained. In alkaline medium, formation of hydroxyl radicals (OH·) is favored by large number of hydroxyl ions (OH^-) that in turn effectively increase the degradation percentage value.

In case of EBT dye, superoxide radical plays the major role in degradation. These are formed when the electrons of conduction band react with adsorbed oxygen molecules as shown in Scheme 1 and Eq. 3 [39]:

$$O_2 + e^- \rightarrow O_2^{\cdot -} \tag{3}$$

$$O_2^{\cdot -} + OH^{\cdot} \rightarrow OH^- + {}^1O_2 \tag{4}$$

Here the highest degradation percentage is observed at low pH value. Decreased percentage values under alkaline conditions are due to the reason that excessive number of hydroxyl radicals convert superoxide radicals to hydroxyl ions (Eq. 4) and hampered the dye degradation process.

In order to further elaborate the impact of pH conditions on catalytic activity of both composites, PZC calculation is considered. PZC for NC1 and NC2 is 7.3 and 6.8 as depicted in Fig. 4.3a, b.

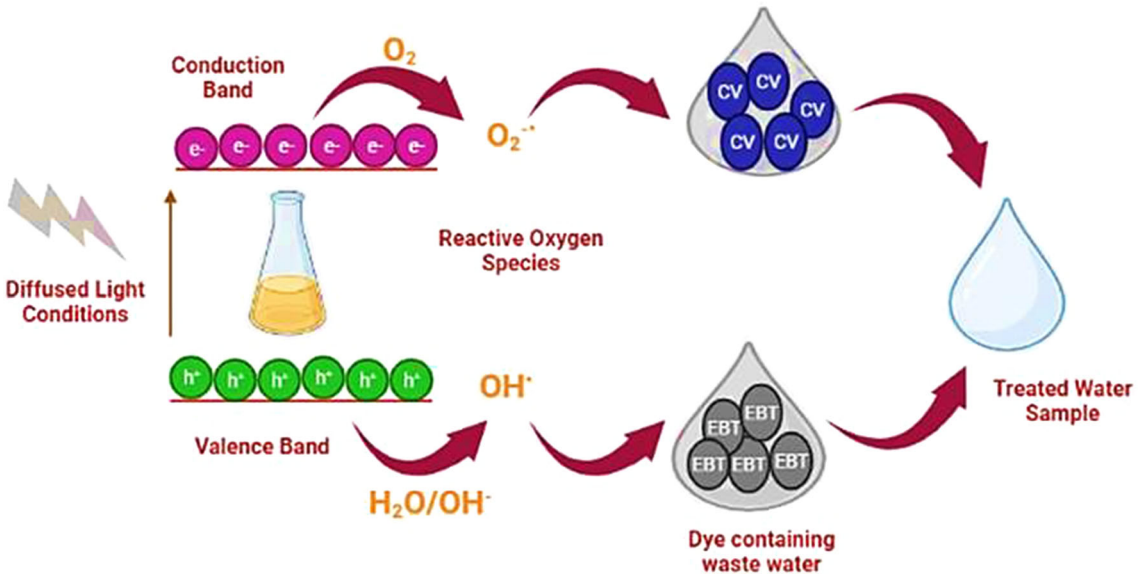

Scheme 1 Formation of reactive species for dye degradation process

In acidic medium (below the PZC value), cationic dye and nanocatalyst developed electrostatic repulsion between them resulting in decreased percentage of dye degradation, while in alkaline medium (above PZC value), the favorable interaction developed between negatively charged nanocatalyst and cationic dye leading to higher degradation percentage. But competition developed at even higher pH values between negatively charged nanocatalyst surface and OH^- ions for dye interaction in the reaction mixture. Moreover, under these conditions, the structure of dye is altered by excessive number of OH^- ions [40].

In acidic medium (below PZC value), the nanocatalyst surface functional groups have been protonated and developed favorable interaction with anionic dye. Alternatively, in alkaline medium (above PZC value), drastic decreased in anionic dye degradation was observed due to negatively charged catalyst surface that imposes repulsion towards anionic dye molecules and OH^- ions within the reaction mixture [1, 41].

3.2.3 Effect of Contact Time and Dye Concentration

In order to optimize the influence of dye concentration and contact time for maximum degradation of crystal violet and eriochrome black T by NC1 and NC2 nanocomposite, 25 mL of dye having varying concentration (5 mg/L, 25 mg/L, 50 mg/L, 75 mg/L and 100 mg/L) was shaken with optimum volume of nanocomposite by keeping other experimental parameters constant. Initially, absorbance values were noted for all dye concentrations at zero time without adding nanocomposite. Then, absorbance taken at regular time intervals of 30, 45, 60, 90, 120 and 180 min for each dye concentration (5 mg/L, 25 mg/L, 50 mg/L, 75 mg/L, and 100 mg/L) is considered as final absorbance value and shown in Fig. 4.4a–d.

In case of CV (Fig. 4.4a, b), both the composite depicted optimum degradation percentage at lower dye concentration value of 5 mg/L within initial 60 (NC1) and 45 min (NC2). On the other hand, in case of EBT (Fig. 4.4c, d), NC1 and NC2 illustrated optimal response within 90 and 60 min for 5 mg/L dye concentration.

It has been observed from the catalytic activity of NC1 or NC2 that increasing dye degradation trend was observed within the time frame of 45–90 min but after achieving maximum degradation, the percentage began to decrease at higher concentration values. Initial incremented degradation was corroborating to the fact that maximum interaction has taken place between dye molecules and reactive species. Higher dye concentration reduces the number of active adsorption sites for hydroxyl ions or oxygen molecules. Further, it decreases the path length of light photons. Both of these factors contribute to the generation of fewer reactive species. This eventually impacts the dye degradation efficiency [1].

3.2.4 Effect of Temperature

Temperature is also crucial and essential parameter to investigate that whether degradation mechanism is exothermic or endothermic in reaction. Factor of temperature is optimized to examine the maximum degrading efficiency of both NC1 and NC2 for cationic-CV and anionic-EBT dyes. Dye degradation was studied at four different temperature values. Initial absorbance (A_i) was measured separately before adding NC1 or NC2 in dye solution. Final absorbance (A_f) was also measured after adding nanocatalyst at their respective maintained

temperature values and shown in Fig. 4.5a, b. Both dyes CV and EBT have shown maximum degradation at room temperature (25 °C) by NC1 or NC2 nanocatalysts. CV has been degraded to 57% and 73%, while EBT has been degraded to 62% and 70% by NC1 and NC2, respectively.

It has been observed that decreasing degradation trend is obtained with increasing temperature for both CV and EBT. At increased temperature, lesser reactive species was generated and lesser interaction was promoted between dye and nanocatalysts. At ambient temperature, increased dye degradation was noted due to exothermic property of nanocatalysts. Availability of more reactive species facilitates interaction at lower temperature values, while higher temperature values may favor the degradation of catalysts. Optimum temperature value of 25 °C has shown efficient and maximum degradation percentages for both CV and EBT [1].

3.2.5 Effect of Interfering Ions

Wastewater comprises various ionic, neutral inorganic species that can influence the catalytic performance of nanocomposites. Effective degradation of dyes was also affected by presence of inorganic salts, and hence, optimized degradation approach has been studied in the presence of these salts.

In order to evaluate the influence of salts on degradation percentage, the effect of various interfering ions such as NaCl, $NaNO_3$ and Na_2CO_3 was explored.

In case of crystal violet, both NC1 and NC2 (Fig. 4.6a) have shown 99% degradation in the absence of interfering ions, while the efficiency of NC1 and NC2 has decreased to 76% (NaCl), 68% ($NaNO_3$), 82% (Na_2CO_3), 60% (NaCl), 71% ($NaNO_3$) and 64% (Na_2CO_3), respectively.

In case of eriochrome black T, as given in Fig. 4.6b, about 73% degradation in the absence of any interfering ions was observed with NC1, while 68%, 54% and 61% percentage was depicted in the presence of NaCl, $NaNO_3$ and Na_2CO_3 salts. Similarly, NC2 has shown about 78% degradation in no interference condition, while 62%, 59% and 71% degradation was shown in the presence of NaCl, $NaNO_3$ and Na_2CO_3 salts. Nitrate and chloride seem to decrease the degradation percentage appreciably. This is due to the fact that nitrate anions can act as hydroxyl radical and electron scavenger, while chloride seems to trap both holes and hydroxyl radicals [42, 43].

3.3 Possible Mechanism of Catalytic Dye Degradation Process

Most appropriate and proposed mechanism of dyes degradation by utilizing biosynthesized nanocatalysts is depicted in Eqs. 5 to 9.

Nanocatalyst being exothermic and reactive in nature when shaken with dye, the heat energy is produced that might be equal or greater than band gap energy of nanocatalyst which eventually stimulated the electrons (e-) in the valence band of nanocatalyst. The stimulated electrons (e-) became excited and transferred to conduction band (CB^{e^-}) of nanocatalyst. This resulted in a vacancy or holes (h^+) in the valance band of nanocatalyst.

$$\text{Nanocatalyst} \rightarrow \text{Nanocatalyst}(CB^{e^-}) + \text{Nanocatalyst}(VB^{h^+}) \quad (5)$$

These positive and negative charge carriers generated within the nanocatalyst undergo redox reaction with water and oxygen available to the nanocatalyst in the reaction mixture. The oxygen molecules undergo reduction reaction by electrons of conduction band (CB^{e^-}) for producing superoxide radical anion ($O_2^{\cdot -}$). The water molecules undergo oxidation reaction with holes (h^+) of the valance band (VB^{h+}) resulting in $OH^{\cdot}$ radical production.

$$\text{Nano catalyst}(CB^{e^-}) + O_2 \rightarrow \text{Nano catalyst}(CB) + O_2^{\cdot -} \quad (6)$$

$$\text{Nano catalyst}(VB^{h^+}) + H_2O/OH^- \rightarrow \text{Nano catalyst (VB)} + OH^{\cdot} \quad (7)$$

Generated radicals $OH^{\cdot}$ and $O_2^{\cdot -}$ being very powerful oxidants undergo further degradation of dyes. Oxidative degradation of CV and EBT resulted in the production of least harmful by-products of mineralization [44–46].

$$\text{Dye (cationic)} + OH^{\cdot} \rightarrow \text{Mineralized products} \quad (8)$$

$$\text{Dye(anionic)} + O_2^{\cdot -} \rightarrow \text{Mineralized products} \quad (9)$$

Further radical scavenging experiment was also carried out to evaluate the significant impact of reactive species formed by nanocomposite on dye degradation procedure. Different scavengers are utilized to trap main reactive species involved in crystal violet and eriochrome black T degradation. In this experiment, iso-propanol (IP), ascorbic acid (AA) and oxalic acid (OA) were considered as quenchers for superoxide radical, hydroxyl radical and holes. The effect of scavengers on degradation of dyes is depicted in Fig. 4.7a, b.

In case of crystal violet dye (Fig. 4.7a), about 99% degradation was observed without scavenger added, while in the presence of IP, AA and OA scavengers, NC1 depicted 72%, 68% and 85% degradation percentage and NC2 illustrated 57%, 49% and 78%, respectively.

In case of eriochrome black T, NC1 has shown 73% degradation in the absence of scavengers, while 48%, 56%

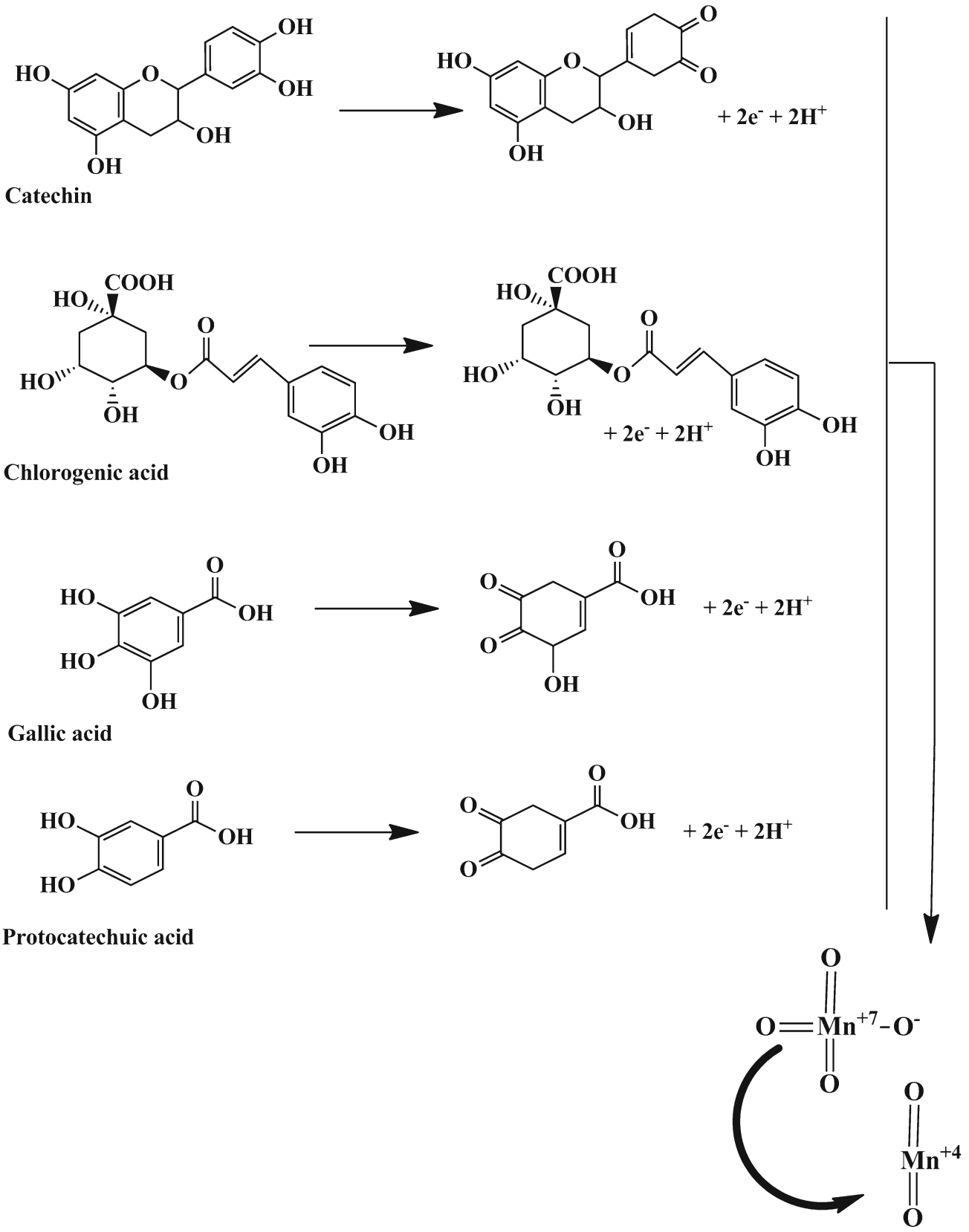

Scheme 2 Synthesis of MnO_2 nanoparticles by *Eucalyptus* phytochemicals

and 62% degradation was observed with IP, AA and OA scavengers, respectively. NC2 has exhibited about 78% degradation in no scavenging condition, while 53%, 58% and 64% with IP, AA and OA, respectively, as depicted in Fig. 4.7b. Superoxide radical and hydroxyl radical are major reactive species responsible for degradation of crystal violet and eriochrome black T [47].

In the end, it can be concluded that nanocomposites have stable nature because these are prepared by combination of two green-synthesized semiconductor material (BCDs (*p*-type) or SCDs (*n*-type) and MnO_2 (intrinsic)). There would be a heterojunction type II structure between the two dissimilar semiconductors. Band gaps of both semiconductors have some potential difference at their junction which resulted in band bending for maintaining the charge carrier's separation efficiently within the nanocomposite. Dopant is used in the preparation of both BCDs- and SCDs-type semiconductors because it could promote the rapid electron excitation from valence band to conduction band and also decrease band gap of both nanocomposites (NC1 and NC2) [45].

3.4 Proposed Pathway for Preparation of Nanoparticles

Eucalyptus citriodora phytochemicals such as catechin, chlorogenic acid, gallic acid and protocatechuic acid under nearly neutral conditions have been oxidized to generate electrons for reduction of MnO_4^- salt solution to MnO_2 nanoparticles. Reduction pathway has been shown in Scheme 2.

4 Conclusion

Biosynthesized nanocomposites based on MnO_2 nanoparticles and boron- or sulfur-doped carbon dots were prepared through green route utilizing *E. citriodora* leaf extract. Comparative influence of different dopant sources on nanocomposite synthesis was investigated through dye degradation studies of crystal violet and eriochrome black T. Results illustrated that optimum degradation of crystal violet (5 mg/L) and eriochrome black T (5 mg/L) was attained with a smaller volume of NC2 in shorter time span. Both nanocomposites proved to be promising candidate for excellent catalytic degradation of dyes. However, NC2 has shown better degradation for both cationic and anionic dye than NC1. This is due to decreased band gap value of NC2 as incorporation of dopant facilitates the upward and downward shift in density of energetically accessible acceptor states of valance and conduction bands. Eventually, it increases the number of carriers in both bands and promotes carrier–carrier interaction.

References

1. Boushehrian, M.M.; Esmaeili, H.; Foroutan, R.: Ultrasonic assisted synthesis of Kaolin/$CuFe_2O_4$ nanocomposite for removing cationic dyes from aqueous media. J. Environ. Chem. Eng. **8**, 103869 (2020). https://doi.org/10.1016/j.jece.fe.103869
2. Selvakumar, T.; Rajaram, M.; Natarajan, A.; Harikrishnan, L.; Alwar, K.; Rajaram, A.: Highly efficient sulfur and nitrogen codoped Graphene quantum dots as a metal-free green hotocatalyst for photocatalysis and fluorescent ink applications. ACS Omega **7**, 12825–12834 (2022). https://doi.org/10.1021/acsomega.2c00092
3. Chauhan, A.K.; Kataria, N.; Garg, V.K.: Green fabrication of ZnO nanoparticles using Eucalyptus spp. leaves extract and their application in wastewater remediation. Chemosphere **247**, 125803 (2020)
4. Rashid, R.; Shafiq, I.; Akhter, P.; Iqbal, M.J.; Hussain, M.: A state-of-the-art review on wastewater treatment techniques: the effectiveness of adsorption method. Environ. Sci. Pollut. Res. **28**, 9050–9066 (2021)
5. Gusain, R.; Gupta, K.; Joshi, P.; Khatri, O.: P: Adsorptive removal and photocatalytic degradation of organic pollutants using metal oxides and their composites: a comprehensive review. Adv. Colloid Interface Sci. **272**, 102009 (2019). https://doi.org/10.1016/j.cis.2019.102009
6. Kumar, M.; Mehta, A.; Mishra, A.; Singh, J.; Rawat, M.; Basu, S.: Biosynthesis of tin oxide nanoparticles using *Psidium guajava* leave extract for photocatalytic dye degradation under sunlight. Mater. Lett. **215**, 121–124 (2018)
7. Javaid, R.; Qazi, U.Y.: Catalytic oxidation process for the degradation of synthetic dyes: an overview. Inter. J. Environ. Res. Public Health **16**, 2066 (2019). https://doi.org/10.3390/ijerph16112066
8. Peng, H.; Guo, J.: Removal of chromium from wastewater by membrane filtration, chemical precipitation, ion exchange, adsorption electrocoagulation, electrochemical reduction, electrodialysis, electrodeionization, photocatalysis and nanotechnology: a review. Environ. Chem. Lett. **18**, 2055–2068 (2020)
9. Zaib, M.; Akhtar, A.; Maqsood, F.; Shahzadi, T.: Green synthesis of carbon dots and their application as photocatalyst in dye degradation studies. Arab. J. Sci. Eng. **46**, 437–446 (2021). https://doi.org/10.1007/s13369-020-04904-w
10. Dhenadhayalan, N.; Lin, K.C.; Saleh, T.A.: Recent advances in functionalized carbon dots toward the design of efficient materials for sensing and catalysis applications. Small **16**, 1905767 (2020). https://doi.org/10.1002/smll.201905767
11. Khayal, A.; Dawane, V.; Amin, M.A.; Tirth, V.; Yadav, V.K.; Algahtani, A.; Jeon, B.H.: Advances in the methods for the synthesis of carbon dots and their emerging applications. Polym. **13**, 3190 (2021). https://doi.org/10.3390/polym13183190
12. Peng, Z.; Zhou, Y.; Ji, C.; Pardo, J.; Mintz, K.J.; Pandey, R.R.; Leblanc, R.M.: Facile synthesis of "boron-doped" carbon dots and their application in visible-light-driven photocatalytic degradation of organic dyes. Nanomaterial **10**, 1560 (2020). https://doi.org/10.3390/nano10081560
13. Luo, K.; Wen, Y.; Kang, X.: Halogen-doped carbon dots: synthesis, application, and prospects. Molecules **27**(14), 4620 (2022). https://doi.org/10.3390/molecules27144620
14. Redondo-Fernandez, G.; Canga, C.J.; Soldado, A.; Encinar, R.J.; Costa-Fernandez, M.J.: Functionalized heteroatom-doped carbon dots for biomedical applications: a review. Anal. Chim. Acta **1284**, 341874 (2023). https://doi.org/10.1016/j.aca.2023.341874
15. Sawalha, H.; Abiri, R.; Sanusi, R.; Shaharuddin, N.A.; Noor, A.A.M.; Ab Shukor, N.A.; Ahmad, S.A.: Toward a better understanding of metal nanoparticles, a novel strategy from Eucalyptus plants. Plants **10**, 929 (2021). https://doi.org/10.3390/plants10050929

16. Qureshi, M.Z.; Bashir, T.; Khursheed, S.; Ismail, T.; Ayub, M.; Reynolds, A.; Hussain, G.: Green synthesis of nanosilver particles from extract of *Eucalyptus citriodora* and their characterization. Asian J. Chem. **26**, 1–3 (2014). https://doi.org/10.14233/AJCHEM.2014.16311
17. Nwabor, O.F.; Singh, S.; Paosen, S.; Vongkamjan, K.; Voravuthikunchai, S.P.: Enhancement of food shelf life with polyvinyl alcohol-chitosan nanocomposite films from bioactive Eucalyptus leaf extracts. Food Biosci. **36**, 100609 (2020). https://doi.org/10.1016/j.fbio.2020.100609
18. Zheng, Y.; Fu, L.; Han, F.; Wang, A.; Cai, W.; Yu, J.; Peng, F.: Green biosynthesis and characterization of zinc oxide nanoparticles using *Corymbia citriodora* leaf extract and their photocatalytic activity. Green Chem. Lett. Rev. **8**, 59–63 (2015). https://doi.org/10.1080/17518253.2015.1075069
19. Joshi, N.C.; Siddiqui, F.; Salman, M.; Singh, A.: Antibacterial activity, characterizations, and biological synthesis of manganese oxide nanoparticles using the extract of aloe vera. Asian Pacific J. Health Sci. **7**, 27–29 (2020). https://doi.org/10.21276/apjhs.2020.7.3.7
20. Kamali, S.R.; Chen, C.N.; Agrawal, D.C.; Wei, T.H.: Sulfur-doped carbon dots synthesis under microwave irradiation as turn-off fluorescent sensor for Cr (III). J. Anal. Sci. Tech. **12**, 1–11 (2021). https://doi.org/10.1186/s40543-021-00298-y
21. Bourlinos, A.B.; Trivizas, G.; Karakassides, M.A.; Baikousi, M.; Kouloumpis, A.; Gournis, D.; Couris, S.: Green and simple route toward boron doped carbon dots with significantly enhanced nonlinear optical properties. Carbon **83**, 173–179 (2015)
22. Guan, J.F.; Huang, Z.N.; Zou, J.; Jiang, X.Y.; Peng, D.M.; Yu, J.: G: A sensitive non- enzymatic electrochemical sensor based on acicular manganese dioxide modified graphene nanosheets composite for hydrogen peroxide detection. Ecotoxic. Environ. Saf. **190**, 110123 (2020). https://doi.org/10.1016/j.ecoenv.2019.110123
23. Bano, D.; Chandra, S.; Yadav, P.K.; Singh, V.K.; Hasan, S.H.: Off-on detection of glutathione based on the nitrogen, sulfur codoped carbon quantum dots@ MnO_2 nano- composite in human lung cancer cells and blood serum. J. Photochem. Photobio. A. Chem. **398**, 112558 (2020). https://doi.org/10.1016/j.jphotochem.2020.112558
24. Zare, M.H.; Mehrabani-Zeinabad, A.: Photocatalytic activity of $ZrO_2/TiO_2/Fe_3O_4$ ternary nanocomposite for the degradation of naproxen: characterization and optimization using response surface methodology. Sci. Rep. **12**, 1–24 (2022). https://doi.org/10.1038/s41598-022-14676-y
25. Soldatova, A.V.; Balakrishnan, G.; Oyerinde, O.F.; Romano, C.A.; Tebo, B.M.; Spiro, T.G.: Biogenic and synthetic MnO_2 nanoparticles: size and growth probed with absorption and Raman spectroscopies and dynamic light scattering. Environ. Sci. Technol. **53**, 4185–4197 (2019). https://doi.org/10.1021/jacs.7b02772
26. Dessie, Y.; Tadesse, S.; Eswaramoorthy, R.: Physicochemical parameter influences and their optimization on the biosynthesis of MnO_2 nanoparticles using *Vernonia amygdalina* leaf extract. Arab. J. Chem. **13**, 6472–6492 (2020). https://doi.org/10.1016/j.arabjc.2020.06.006
27. Garg, D.; Mehta, A.; Mishra, A.; Basu, S.: A sensitive turn on fluorescent probe for detection of biothiols using MnO_2@ carbon dots nanocomposites. Spectrochim. Acta. Part A Mol. Biomol. Spec. **192**, 411–419 (2018)
28. Shen, J.; Shang, S.; Chen, X.; Wang, D.; Cai, Y.: Facile synthesis of fluorescence carbon dots from sweet potato for Fe^{3+} sensing and cell imaging. Mater. Sci. Eng. **76**, 856–864 (2017). https://doi.org/10.1016/j.msec.2017.03.178
29. Sahu, V.; Khan, F.: Synthesis of bovine serum albumin capped boron-doped carbon dots for sensitive and selective detection of Pb (II) ion. Heliyon **6**, e03957 (2020). https://doi.org/10.1016/j.heliyon.2020.e03957
30. Nemati, F.; Hosseini, M.; Zare-Dorabei, R.; Salehnia, F.; Ganjali, M.R.: Fluorescent turn on sensing of caffeine in food sample based on sulfur-doped carbon quantum dots and optimization of process parameters through response surface methodology. Sens. Actuator B: Chem. **273**, 25–34 (2018). https://doi.org/10.1016/j.snb.2018.05.163
31. Kang, Y.G.; Yoon, H.; Lee, C.S.; Kim, E.J.; Chang, Y.S.: Advanced oxidation and adsorptive bubble separation of dyes using MnO_2-coated Fe_3O_4 nanocomposite. Water Res. **151**, 413–422 (2019)
32. Meena, P.L.; Poswal, K.; Surela, A.K.; Saini, J.K.: Facile synthesis of $ZnO/CuO/Ag_2O$ ternary metal oxide nanocomposite for effective photodegradation of organic water pollutants. Water Sci. Technol. **84**, 2615–2634 (2021). https://doi.org/10.2166/wst.2021.431
33. Naik, V.M.; Gunjal, D.B.; Gore, A.H.; Pawar, S.P.; Mahanwar, S.T.; Anbhule, P.V.; Kolekar, G.B.: Quick and low cost synthesis of sulphur doped carbon dots by simple acidic carbonization of sucrose for the detection of Fe^{3+} ions in highly acidic environment. Diam. Relat. Mater. **88**, 262–268 (2018). https://doi.org/10.1016/j.diamond.2018.07.018
34. Patel, J.; Singh, A.K.; Jain, B.; Yadav, S.; Carabineiro, S.A.; Susan, M.A.B.H.: Solochrome dark blue azo dye removal by sonophotocatalysis Using Mn^{2+} doped ZnS quantum dots. Catalysts **11**, 1025 (2021). https://doi.org/10.3390/catal11091025
35. Mondal, D.; Das, S.; Paul, B.K.; Bhattacharya, D.; Ghoshal, D.; Gayen, A.L.; Das, S.: Size engineered Cu-doped α-MnO_2 nanoparticles for exaggerated photocatalytic activity and energy storage application. Mater. Res. Bull. **115**, 159–169 (2019). https://doi.org/10.1016/j.materresbull.2019.03.023
36. Mohammed, A.; Abdullah, A.: Scanning electron microscopy (SEM): a review. Inter. Conf. Hydraul. Pneum. **7**, 1–9 (2018)
37. He, X.; Li, Y.; Yang, C.; Lu, L.; Nie, Y.; Tian, X.: Carbon dots–MnO_2 nanocomposites for As (iii) detection in groundwater with high sensitivity and selectivity. Anal. Methods **12**, 5572–5580 (2020). https://doi.org/10.1039/d0ay01846e
38. Shokri, R.; Amjadi, M.: A ratiometric fluorescence sensor for triticonazole based on the encapsulated boron-doped and phosphorous-doped carbon dots in the metal organic framework. Spectrochim Acta Part A Mol. Biomol. Spec. **246**, 118951 (2021). https://doi.org/10.1016/j.saa.2020.118951
39. Zhao, J.; Xiao, P.; Han, S.; Zulhumar, M.; Wu, D.: Preparation of magnetic copper ferrite nanoparticle as peroxymonosulfate activating catalyst for effective degradation of levofloxacin. Water Sci. Technol. **85**(2), 645–663 (2022). https://doi.org/10.2166/wst.2021.627
40. Chiam, S.L.; Pung, S.Y.; Yeoh, F.Y.: Recent developments in MnO_2-based photocatalysts for organic dye removal: a review. Environ. Sci. Pollut. Res. **27**, 5759–5778 (2020). https://doi.org/10.1007/s11356-019-07568-8
41. Baruah, M.; Supong, A.; Bhomick, P.C.; Karmaker, R.; Pongener, C.; Sinha, D.: Batch sorption–photodegradation of Alizarin Red S using synthesized TiO_2/activated carbon nanocomposite: an experimental study and computer modelling. Nanotechnol. Environ. Eng. **5**, 1–13 (2020). https://doi.org/10.1007/s41204-020-00071-3
42. Ahmed, S.; Rasul, M.G.; Martens, W.N.; Brown, R.; Hasib, M.A.: Advances in heterogeneous photocatalytic degradation of phenols and dyes in wastewater: A Review. Water Air Soil Pollut. **215**, 3–29 (2011). https://doi.org/10.1007/s11270-010-0456-3
43. Cavicchioli, A.; Gutz, I.G.R.: Effect of scavengers on the photocatalytic digestion of organic matter in water samples assisted by TiO_2 in suspension for the voltammetric determination of heavy metals. J. Braz. Chem. Soc. **13**(4), 441–448 (2002). https://doi.org/10.1590/S0103-50532002000400006
44. Abbas, H.A.; Nasr, R.A.; Abu-Zurayk, R.; Al Bawab, A.; Jamil, T.S.: Decolourization of crystal violet using nano-sized novel fluorite structure $Ga_2Zr^{2-}xWxO_7$ photocatalyst under visible light

irradiation. R. Soc. Open Sci. **7**, 191632 (2020). https://doi.org/10.1098/rsos.191632
45. Rani, M.; Shanker, U.: Synergistic effects of zinc oxide coupled copper hexacyanoferrate nanocomposite: robust visible-light driven dye degradation. J. Colloid Interface Sci. **584**, 67–79 (2021). https://doi.org/10.1016/j.jcis.2020.09.079
46. Kumari, V.; Kaushal, S.; Singh, P.P.: Green synthesis of a CuO/rGO nanocomposite using a *Terminalia arjuna* bark extract and its catalytic activity for the purification of water. Mater. Adv. **3**, 2170–2184 (2022). https://doi.org/10.1039/D1MA00993A
47. Santhosh, C.; Malathi, A.; Daneshvar, E.; Kollu, P.; Bhatnagar, A.: Photocatalytic degradation of toxic aquatic pollutants by novel magnetic 3D-TiO_2@ HPGA nanocomposite. Sci. Rep. **8**, 1–15 (2018). https://doi.org/10.1038/s41598-018-33818-9